OPEN

Correspondence and
requests for materials
should be addressed to
Y.Y.L. (liyynano@hust.
edu.cn) or J.P.L. (liujp@
mail.ccnu.edu.cn)

Directly Grown Nanostructured Electrodes for High Volumetric Energy Density Binder-Free Hybrid Supercapacitors: A Case Study of CNTs//Li$_4$Ti$_5$O$_{12}$

Wenhua Zuo[1], Chong Wang[1], Yuanyuan Li[2] & Jinping Liu[1]

[1]Institute of Nanoscience and Nanotechnology, Department of Physics, Central China Normal University, Wuhan 430079, Hubei, P.R. China, [2]School of Optical and Electronic Information, Huazhong University of Science and Technology, Wuhan 430074, P. R. China.

Hybrid supercapacitor (HSC), which typically consists of a Li-ion battery electrode and an electric double-layer supercapacitor electrode, has been extensively investigated for large-scale applications such as hybrid electric vehicles, etc. Its application potential for thin-film downsized energy storage systems that always prefer high volumetric energy/power densities, however, has not yet been explored. Herein, as a case study, we develop an entirely binder-free HSC by using multiwalled carbon nanotube (MWCNT) network film as the cathode and Li$_4$Ti$_5$O$_{12}$ (LTO) nanowire array as the anode and study the *volumetric energy storage capability*. Both the electrode materials are grown directly on carbon cloth current collector, ensuring robust mechanical/electrical contacts and flexibility. Our 3 V HSC device exhibits maximum volumetric energy density of ∼4.38 mWh cm^{-3}, much superior to those of previous supercapacitors based on thin-film electrodes fabricated directly on carbon cloth and even comparable to the commercial thin-film lithium battery. It also has volumetric power densities comparable to that of the commercial 5.5 V/100 mF supercapacitor (can be operated within 3 s) and has excellent cycling stability (∼92% retention after 3000 cycles). The concept of utilizing binder-free electrodes to construct HSC for thin-film energy storage may be readily extended to other HSC electrode systems.

Lithium ion battery (LIB) and supercapacitor are two key components in typical energy storage systems[1–3]. The most important difference between LIB and supercapacitor is that, in a certain volume, LIB could store dozens of times more energy than supercapacitor while supercapacitor could deliver hundreds of times and even more power than LIB. They have been widely utilized to power most of portable electronics and small machines[4,5], and have attracted enormous attention in hybrid vehicles and even smart electrical grid[6]. With such ever-growing energy needs, single typical LIB or supercapacitor cannot work well[7], and researchers are striving to develop energy storage materials and systems which possess both high energy and power densities[8]. For LIB, in order to enhance its power density, great attempts have been made to improve the electrical and ionic conductivity of electrodes by designing appropriate micro-/nanostructures[9–12]. While for supercapacitor, much work has been done to look for highly capacitive materials or asymmetric supercapacitor systems to increase the capacitance and working potential window, eventually to increase the energy density[13–22].

As an alternative technology to LIB and supercapacitor, hybrid supercapacitor (HSC), which typically consists of a Li-ion battery-type electrode and an electric double-layer supercapacitor electrode (such as graphene$_{(+)}$// Fe$_3$O$_{4(-)}$[23],AC$_{(+)}$//Ti-based oxide$_{(-)}$[24,25],LiMn$_2$O$_{4(+)}$//AC$_{(-)}$[26,27],AC$_{(+)}$//V$_2$O$_{5(-)}$[28]), combines the advantages of both LIB and supercapacitor[29,30]. Firstly, compared to traditional supercapacitor, HSC generally utilizes non-aqueous electrolyte like in LIBs, enabling a wider working potential window[31]; the battery-type electrode also provides larger capacity than typical capacitive materials. These two aspects ensure a much higher energy density. Secondly, when compared with LIB, the electric double-layer electrode promotes the power capability and cycling stability[32]. As a result, HSC has opened a new avenue for emerging energy-storage applications such as electric

vehicles. It can bridge up the gap between LIB and supercapacitor and in some cases can even achieve energy comparable to LIB and power comparable to traditional supercapacitor. Despite this, the battery electrode in HSC still suffers sluggish ion diffusion at high rates and pulverization upon long-term cycling. To address this challenge, the most popular way is to develop the battery electrodes hybridized with various carbon nanomaterials (activated carbon, carbon nanotube, graphene, etc.)[23,25,28,33,34]. The integrated carbon materials work as structure backbones, electron transport pathways or even as capacitive materials to enhance the charge storage rate and capacitance[35]. So far, the main attention on HSC has been paid to construct such high-rate battery electrodes and great progress has been made in obtaining high gravimetric energy and power densities for large-scale applications.

For applications in smart portable, flexible and wearable electronics as well as micro-/nano-electromechanical systems, however, the energy storage devices should be miniaturized in dimension and boosted in mechanical flexibility[33,36–39]. In such cases, energy is stored in limited space/area and the performance metrics concerned are mainly volumetric energy and power densities. Although thin-film LIB and supercapacitor technologies provide possible solutions, they in general could not simultaneously provide high energy and power (the volumetric energy density of traditional supercapacitors is in most cases ≤ 1 mWh cm^{-3} and the volumetric power density of commercial thin-film lithium batteries is ≤ 5 mW cm^{-3})[7,40]; the energy supply systems in these application fields have been requiring a greater degree of development. In this regard, HSC opens up a new opportunity. However, to our knowledge, its volumetric energy storage capability has never been investigated for downsized energy storage systems.

In the present work, we make the first attempt to construct a thin-film HSC with both high volumetric energy and power densities. Both the cathode and anode are entirely binder-free, and the active nanomaterials are growing directly on current collector substrate, very different from previous slurry-processed HSC electrodes[29,30,41]. The direct growth of nanostructures on current collector represents a popular way to fabricate thin-film electrodes, which not only ensures convenient electron transport channels and ion diffusion pathways, but also provides sufficient structural interspaces for buffering volume expansion of the battery electrode[11,33,42–53]. When combined with flexible current collector, such thin-film electrode also has greater durability to shape deformation, giving better mechanical flexibility. As a case study, we choose multiwalled carbon nanotube (MWCNT) network film as the cathode and Li$_4$Ti$_5$O$_{12}$ (LTO) nanowire array as the anode; both are grown directly on carbon cloth current collector. The highly-conductive MWCNT network film facilitates the direct contact with electrolyte, capable of providing high double-layer capacitance; while LTO as the battery-type electrode is "zero-strain" and highly safe[54–57]. As a result, our full-cell HSC device exhibits a high volumetric energy density up to ~ 4.38 mWh cm^{-3} and the maximum volumetric power density (~ 565 mW cm^{-3}, charge/discharge within 3 s) approaching that of the commercially available supercapacitors. The energy density value is comparable to that of commercial 4 V–500 μAh thin-film lithium batteries and is much superior to those of all recently reported symmetric/asymmetric supercapacitors based on thin-film electrodes fabricated directly on carbon cloth. Our HSC also shows a stable cycling behavior up to 3000 times. The present work clearly demonstrates that binder-free HSC is promising in thin-film downsized energy storage systems.

Results

Figure 1 shows the schematic illustration of our HSC configuration. The LTO array works as the popular insertion anode characteristic of long life and high safety while MWCNT network film serves as the cathode providing large ion-accessible surface area for double-layer
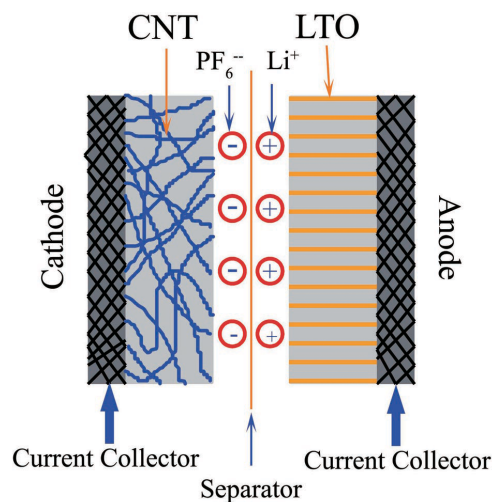

Figure 1 | Schematic illustration of our binder-free HSC structure.

capacitance; both electrodes are grown directly on a highly porous and conductive carbon cloth without any binder and additive. It is noted that in cathode's high potential range, MWCNT does not intercalate lithium as in traditional LIBs where it was used as anode. The electrolyte and separator are the same to that in traditional LIBs.

Characterizations of LTO array anode and MWCNT film cathode. Through a facile hydrothermal process, RTO nanowire array was attained homogeneously on each fiber of carbon cloth (Figure 2a,b). The nanowires in general have needle-like tips and very smooth surface with diameters distributed between 70 and 150 nm (Figure 2c). The RTO nanowire array was converted into LTO nanowire array via a high-temperature solid-state reaction: $5RTO + 4LiOH \rightarrow Li_4Ti_5O_{12} + 2H_2O$. The conversion from RTO to LTO is different from previous cases that LTO was obtained from anatase TiO$_2$ and layered titanate[54–58], and our case is believed to be more facile since the conversion from tetragonal to cubic structure is energetically favorable. After dropping LiOH into RTO nanowire array and drying, the RTO nanowire array is found to be fully covered by LiOH microcrystals (Figure 2d$_1$). The microcrystal is excess after the conversion reaction (Figure 2d$_2$), and the LTO nanowires can be exposed only after LiOH removal (Figure 2d$_3$). Figure 2e and f clearly demonstrate that the morphology of the nanowire array could be well maintained after conversion (~ 4–4.5 μm in length). The nanowires' diameter expands more than 20 nm, and the most morphology difference between RTO and LTO nanowires is that the surface of LTO nanowires becomes rough (Figure 2g). The presence of protrusions on the LTO nanowires is due to the structure reorganization during the phase transformation.

XRD patterns of the components on carbon cloth correspond well with the morphology evolution as discussed above (Figure 3). It is observed that the dominant component of the nanowire array is spinel cubic-phase LTO after solid-state reaction (JCPDS Card No. 49-0207). Small peaks from tetragonal RTO (JCPDS Card No. 1-1292) can still be detected even though LiOH is excess, indicating that the conversion is not complete in our case. Based on the weight loss before and after the excess LiOH removal, the weight percentage of RTO in the LTO array was calculated to be ca. 8–10%. LTO nanowire array was further investigated by TEM observation and the results are shown in Figure 4. Pure-phase LTO nanowires can be detected (Figure 4a,b), the interplanar spacing of 0.48 nm corresponds to (111) plane of spinel LTO. In addition, partially converted RTO nanowires with LTO layer on the surface are also found, as displayed in Figure 4c. The observed d-spacing of 0.32 nm matches
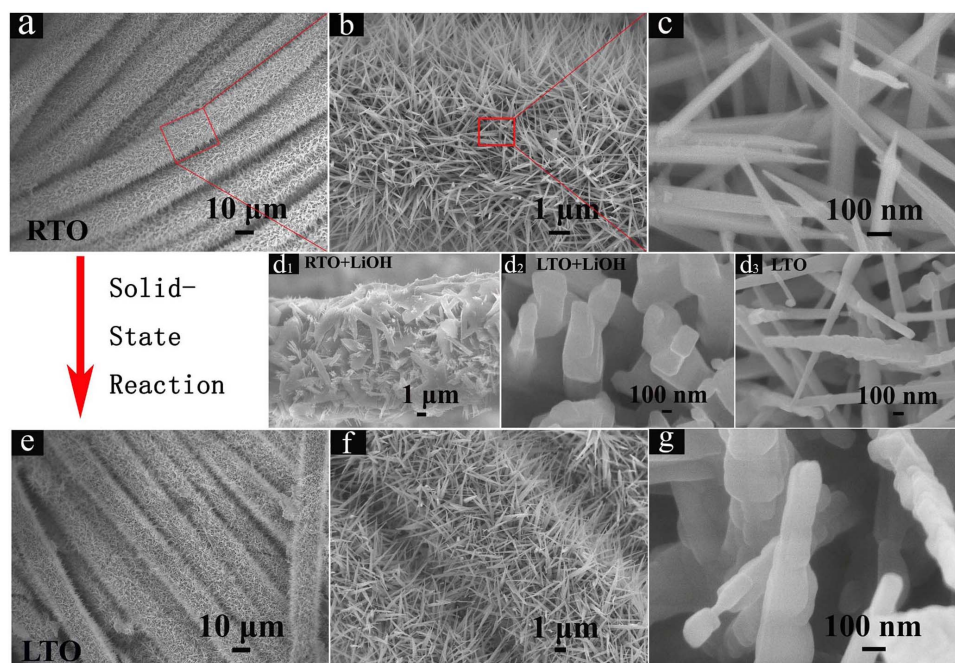
Figure 2 | (a–c) SEM images of the RTO nanowire array with different magnifications. (d_1) RTO nanowire array with LiOH before calcination, showing that LiOH microcrystals cover fully on the array. (d_2) LTO nanowire array covered by excess LiOH after calcination. (d_3) Pure LTO array with clean surface. (e–g) SEM images of the LTO nanowire array with different magnifications.

well with that of (110) plane of tetragonal RTO (Figure 4d). The outer LTO exhibits clear crystal lattice with bright fast Fourier transform (FFT) patterns, indicating the high-quality single-crystalline nature of LTO (Figure 4e and inset). Based on the TEM results, it is proposed that the presence of remaining RTO in the LTO array anode should be due to relatively large diameters of some RTO nanowires, which make the diffusion of LiOH into the inner RTO part difficult at the last stage of the conversion process.

Figure 5a and b show SEM images of the MWCNT film cathode. The MWCNTs grow on carbon cloth fiber uniformly and tightly with the film thickness of $\sim$5–10 µm. Both cross-sectional and top-view images demonstrate that the MWCNTs are curving and interconnected with each other, forming highly porous network morphology.
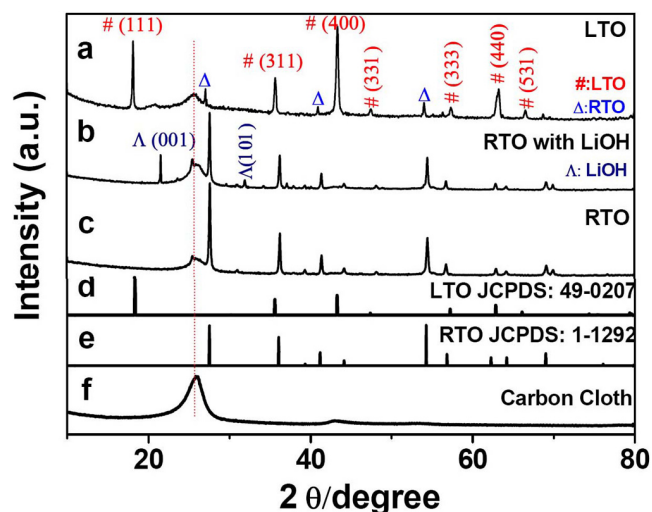
TEM image in Figure 5c further reveals the tubular and multiwalled structure of the CNTs; the outer diameters are $\sim$20–35 nm and the inner diameters are $\sim$10–15 nm. High-resolution TEM image (Figure 5d) clearly shows an interplanar spacing of 0.34 nm, corresponding to (002) planes of MWCNTs.

Electrochemical testing of half cells. For small-scale thin-film energy storage application, the capability of storing more energy

Figure 3 | XRD patterns of (a) LTO nanowire array, (b) RTO nanowire array with LiOH before calcination, (c) RTO nanowire array and (f) carbon cloth. The standard XRD patterns of LTO and RTO are also shown in (d) and (e) respectively for reference.
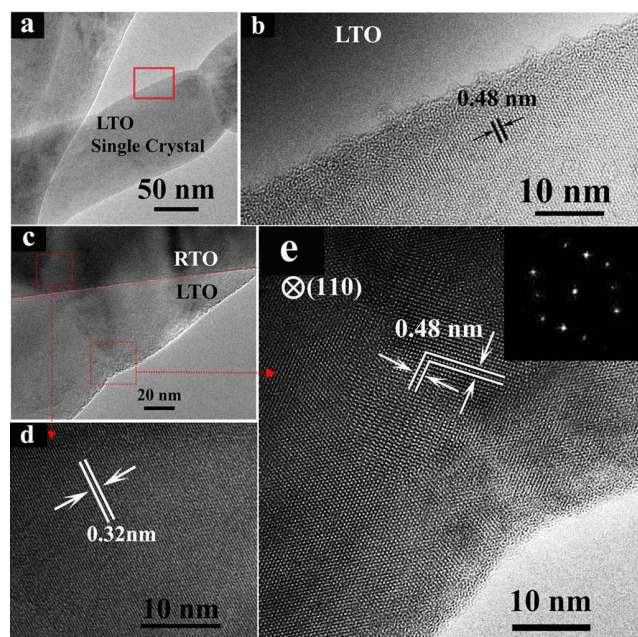

Figure 4 | (a, b) Low and high-resolution TEM images of pure-phase LTO single-crystalline nanowires. (c) TEM image of an individual LTO nanowire with remaining RTO inside. (d) High-resolution TEM image of the inner RTO. (e) High-resolution TEM image of the outer LTO with the inset showing the corresponding FFT.
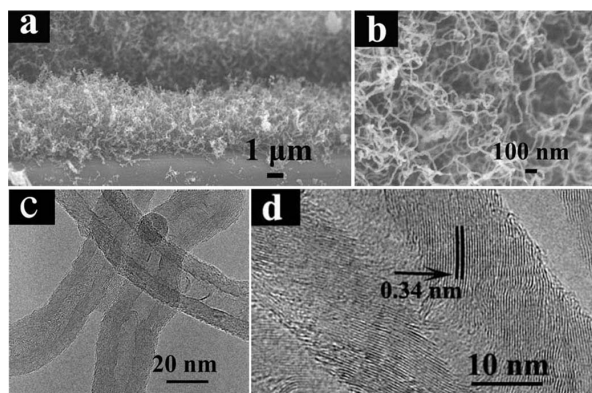
Figure 5 | (a) Cross-sectional and (b) top-view SEM images of MWCNT network film cathode. (c, d) TEM and high-resolution TEM images of MWCNTs.

per unit area/volume is required. Therefore, different from all previous publications on HSCs, we will mainly report on the areal capacity/capacitance and volumetric energy/power densities in this and next sections. Also, the corresponding gravimetric data will be given for reference, especially in rate capability figures. Before constructing a full-cell HSC device, we examined the energy storage performance of directly-grown LTO anode and MWCNT cathode in Li half cells over 1–2.5 V and 3–4 V, respectively.

Figure 6a shows the cyclic voltammetry (CV) analysis of LTO//Li half cell at a scan rate of 5 mV s^{-1}. A pair of peaks can be detected, corresponding to the redox reactions associated with Li$^+$ insertion/extraction[54]. Figure 6b illustrates the CV curve of MWCNT//Li half

cell at 10 mV s^{-1}. The almost rectangular shape of the CV is indicative of pure capacitive energy storage, which is due to the electrolyte ions' accumulation on MWCNT surface (forming electric double layer). The battery behavior of LTO anode and capacitive behavior of MWCNT cathode are further demonstrated by galvanostatic charge/discharge curves, as shown in Figure 6c and d, respectively. It is obvious that the LTO anode exhibits a flat charge/discharge plateau around 1.55 V, mainly characteristic of the two phase equilibrium between LTO and Li$_7$Ti$_5$O$_{12}$ (Li$_4$Ti$_5$O$_{12}$+3Li$^+$+3e$^-$ $\Leftrightarrow$ Li$_7$Ti$_5$O$_{12}$)[59,60]. In contrast, the charge and discharge curves of MWCNT cathode have a triangular shape with linear voltage-time plots (a non-faradic process). Based on the above analysis and the structure of our HSC in Figure 1, the energy storage mechanism can be elucidated as follows: During the charging process, Li$^+$ cations from the electrolyte are inserted into LTO anode to form Li$_7$Ti$_5$O$_{12}$, at the same time, PF$_6^-$ anions are adsorbed on the surface of MWCNT cathode, forming electric double layer with positive charges. When discharged, Li$^+$ are deinserted from Li$_7$Ti$_5$O$_{12}$ while PF$_6^-$ anions are desorbed from the MWCNT surface, both Li$^+$ and PF$_6^-$ eventually return back into the electrolyte.

To assemble a full-cell supercapacitor, it is necessary to make sure that the stored charge in anode (Q_-) is equal to that in cathode (Q_+)[20]. To this end, we have already optimized the experimental details to grow appropriate amount of MWCNT cathode. It was found that the stored charge in cathode increased with increasing the growth times of MWCNT film and five times-repeated growth could achieve good charge balance with the LTO anode. In Figure 7, the quantities of charges stored in both anode and optimized cathode at various current densities are compared. We call Figure 7 as "matching map", from which one can see the overall performance of each electrode and determine if the resulting full cell will behave
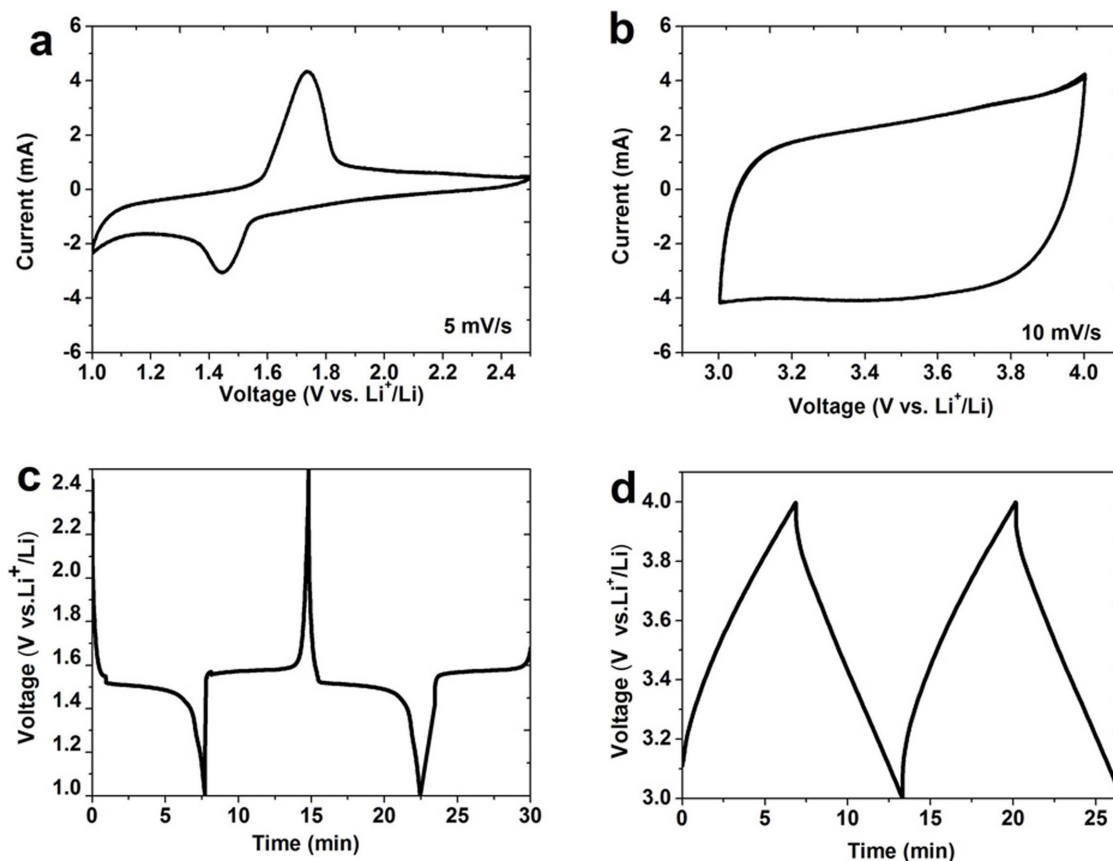

Figure 6 | CV analysis of (a) LTO//Li half cell and (b) MWCNT//Li half cell. Typical charge-discharge curves of (c) LTO//Li half cell and (d) MWCNT//Li half cell at 1 mA cm^{-2}.
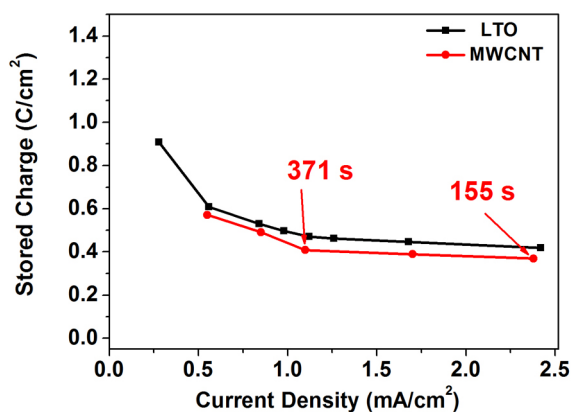
Figure 7 | Matching map of LTO anode and optimized MWCNT cathode, showing the relationship between stored charge and current density.

well. As can be seen, LTO anode can store charge of 0.61, 0.53, 0.47, 0.45, and 0.42 C cm^{-2} at a current density of 0.56, 0.84, 1.12, 1.68, 2.42 mA cm^{-2}, respectively, and MWCNT cathode stores charge of 0.57, 0.49, 0.41, 0.39, and 0.37 C cm^{-2} at 0.55, 0.85, 1.1, 1.7, 2.38 mA cm^{-2}, respectively. Thus, the two electrodes are highly matched, which store approximate charge Q at similar current densities, exhibiting comparable rate capability.

The detailed rate performance and cycling stability of LTO anode and MWCNT cathode are further investigated in Figure 8. In Figure 8a and c, both the areal and gravimetric capacities/capacitances are provided. It can be seen that the two electrodes demonstrate good rate capability and show stable capacity/capacitance at each current density. LTO//Li half cell was charged and discharged for 400 cycles at a current density of 0.4 mA cm^{-2}, the cycling behavior is presented in Figure 8b. It is obvious that LTO could deliver capacity of ~0.235 mAh cm^{-2} and retain 95% of the initial value

after 400 cycles. The cycling performance of MWCNT was carried out at 0.6 mA cm^{-2} and the result is illustrated in Figure 8d. In this case, the charge/discharge capacitance of MWCNT is estimated to be ~ 0.44 F cm^{-2}, which decreases less than 4% after 160 cycles. The corresponding gravimetric capacitance is ca. 109 F g^{-1} (even reach 125 F g^{-1} at 0.55 mA cm^{-2}). As far as we know, such a value is large for CNTs measured in organic electrolyte[22] and is probably related to the microstructure of our MWCNT. From the HRTEM image in Figure 5d, there is in general a certain angle between the graphitic layers and the axis direction of MWCNT. It is thus believed that there are more active sites on the MWCNT's surface for charge accumulation due to the opened edges of graphitic layers to electrolyte. From Figure 8b and d, both LTO and MWCNT electrodes also have high coulombic efficiency approaching 100% after extended cycles.

Electrochemical characterization of HSC device. Using carbon cloth current collector to support the growth of LTO nanowire array anode and MWCNT network film cathode endows our HSC device with good flexibility, as illustrated in Figure 9a. Figure 9b shows the selected charge-discharge profiles of the HSC at different current densities ranging from 0.56 to 9.41 mA cm^{-2}. Our HSC can be operated within a large potential window of 0–3 V, which consists well with the half-cell potential ranges of LTO and MWCNT. The charge-discharge curves exhibit an almost triangular shape with relatively linear voltage-time plots, revealing good capacitive behavior. The cycling response at continuously variable currents (powers) was further evaluated and shown in Figure 9c. In Figure 9c, the current density and capacitance have been converted into power density and energy density, respectively. Five power densities were adopted and our HSC shows stable performance at each step (tens of cycles). When the power density turns back to 27, 18 and 13.5 mW cm^{-3} (corresponding to 1.125, 0.75 and 0.56 mA cm^{-2}), the cell's energy density is fully recovered to the original values, demonstrating that the HSC can be operated continuously at different rates without destructing the cell. The highest volumetric energy density is
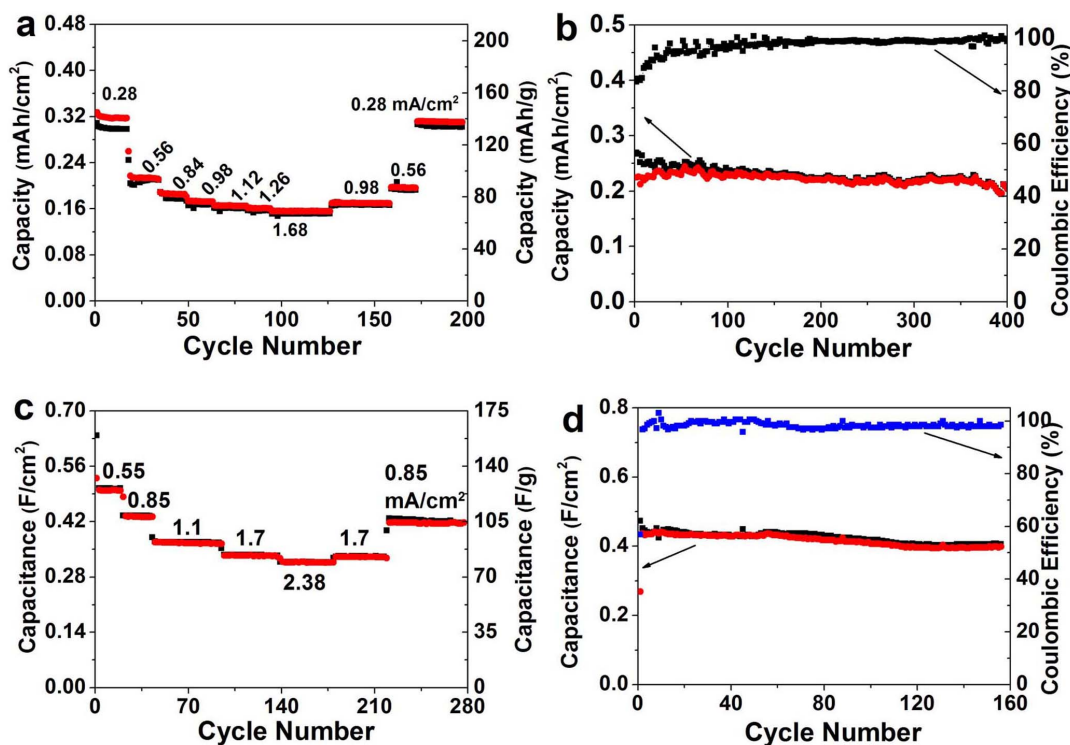

Figure 8 | (a) Rate capability and (b) Cycling performance (at 0.4 mA cm^{-2}) of LTO//Li half cell. (c) Rate capability and (d) Cycling performance (at 0.6 mA cm^{-2}) of MWCNT//Li half cell.
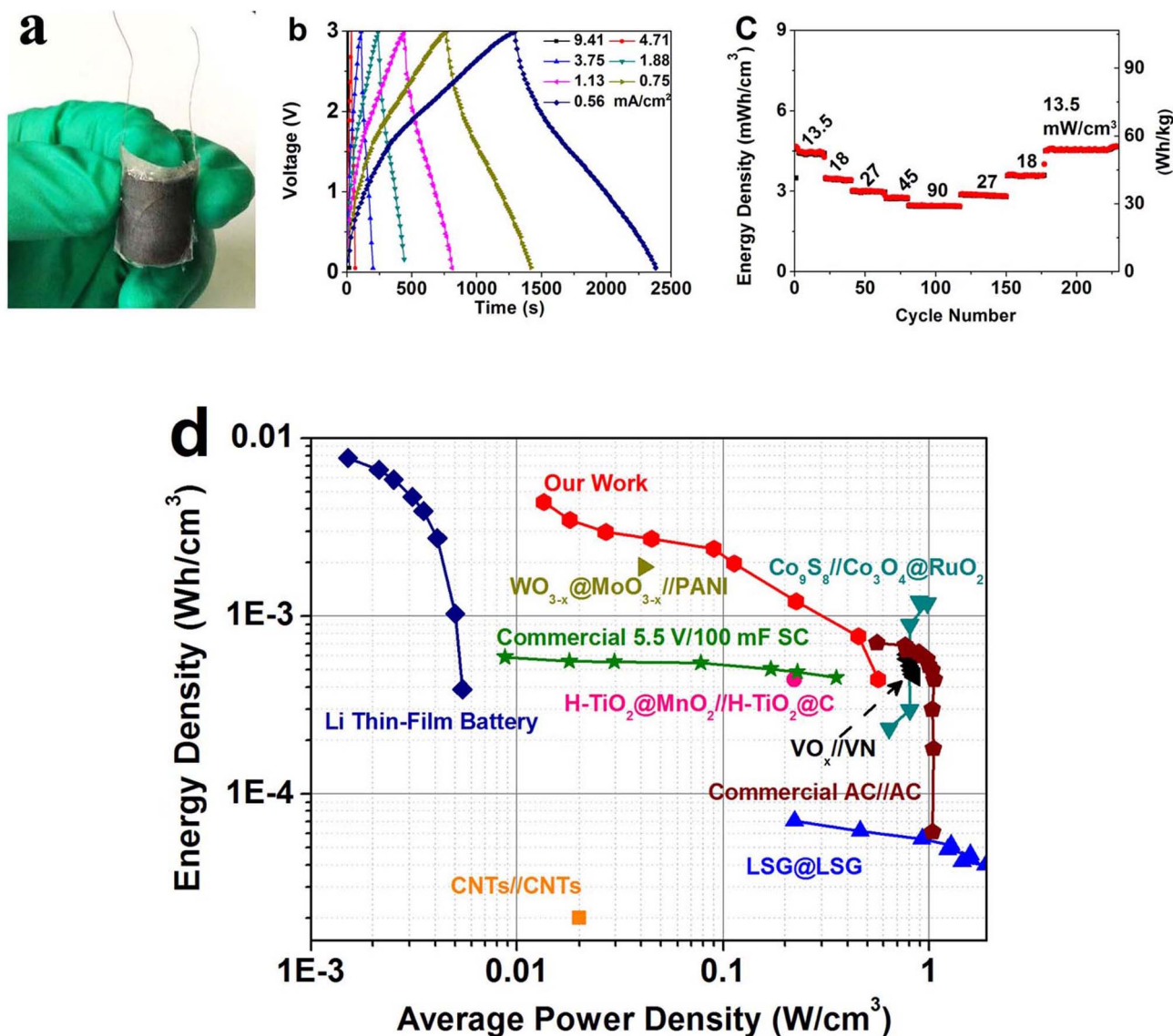
Figure 9 | (a) Optical image of our HSC. (b) Charge-discharge curves of device at various current densities. (c) The cycling response at continuously variable currents (powers). (d) Volumetric energy and powder densities of our HSC device compared with other data. Data for laser-scribed graphene (LSG) supercapacitor, Li thin-film battery and commercial AC//AC supercapacitor are reproduced with permission from ref. 7. Data for commercial 5.5 V/100 mF supercapacitor is reproduced from ref. 8.

$\sim$4.38 mWh cm^{-3}, corresponding to a gravimetric energy density of $\sim$54 Wh kg^{-1}. This gravimetric value is high and comparable to that of most previous HSCs[23–28].

In order to manifest the superiority of our HSC for downsized energy storage, Ragone plot of volumetric energy density versus power density is presented and compared with previous supercapacitor data as well as those of commercially available state-of-the-art energy storage systems (Figure 9d). In general, our HSC device has high volumetric energy densities, even comparable to the commercial thin-film lithium battery (0.3–10 mWh cm^{-3}). The highest energy density (4.38 mWh cm^{-3}) is about several times higher than that of commercially available supercapacitors (such as AC//AC and 5.5 V/100 mF, <1 mWh cm^{-3}) and two orders of magnitude higher than that of reported nanocarbon-based symmetric supercapacitors including CNTs//CNTs[53] and laser-scribed graphene(LSG)//LSG[7], etc. This maximum energy density value is also much superior to those of most typical asymmetric supercapacitors based on thin-film electrodes fabricated directly on carbon cloth, such as H-TiO$_2$@MnO$_2$//H-TiO$_2$@C ($\sim$0.3 mWh cm^{-3})[13], WO$_{3-x}$@MoO$_{3-x}$//PANI ($\sim$1.9 mWh cm^{-3})[50], Co$_9$S$_8$//Co$_3$O$_4$@RuO$_2$ ($\sim$1.21 mWh cm^{-3})[17],

VO$_x$//VN ($\sim$0.61 mWh cm^{-3})[52] and MnO$_2$//Fe$_2$O$_3$($\sim$0.55 mWh cm^{-3})[18]. The maximum volumetric power density for our HSC is $\sim$565 mW cm^{-3}, comparable to the commercial 5.5 V/100 mF supercapacitor and approaching that of AC//AC supercapacitor. It is also two orders of magnitude higher than that of commercially available lithium thin-film batteries. At such a power density, the HSC was charged and discharged within 3 s and still exhibits a high energy density of 0.44 mWh cm^{-3}.

Discussion

The cycling stability of our HSC at a constant current density of 0.65 mA cm^{-2} was also evaluated, as shown in Figure 10a. At the beginning of the cycling, our cell shows an energy density of 3.85 mWh cm^{-3}. The energy density still remains 3.55 mWh cm^{-3} after 3000 cycles, demonstrating 92% retention; that means the energy density decay per cycle is only $\sim$0.0027%. The coulombic efficiency increases with increasing the cycle times, from initial 94.0% to final 99.4%, which indicates the excellent electrochemical reversibility of the HSC. Inset in Figure 10a displays the charge-discharge curves for the last 10 cycles. It is obvious that pure and
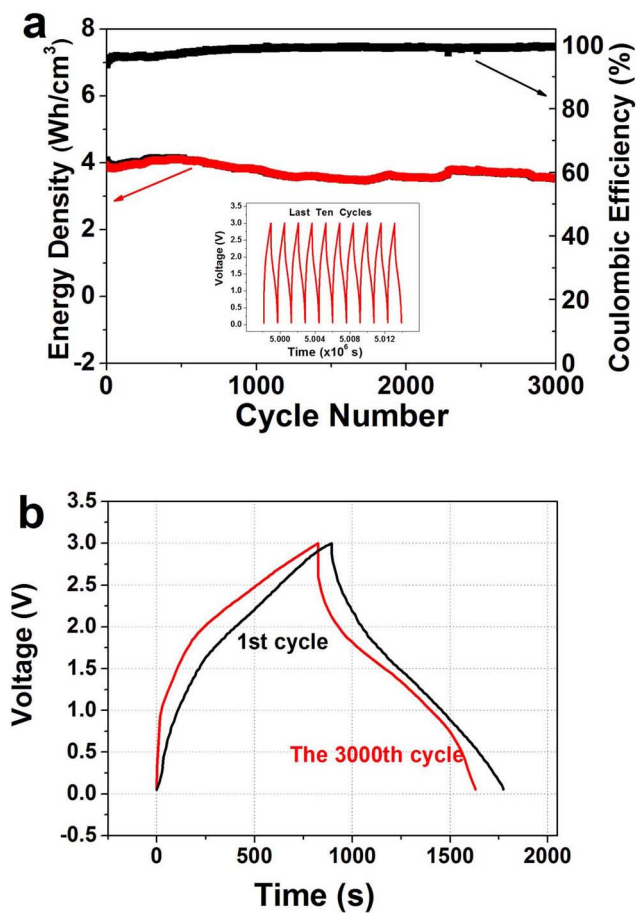
Figure 10 | (a) Cycling performance of our HSC device at 0.65 mA cm⁻². Inset is the charge-discharge curves for the last 10 cycles. (b) The charge-discharge curves of the first and the 3000th cycle.

stable capacitive behavior can be maintained for our HSC after long-term cycling within 0–3 V. Minor difference between the charge-discharge curves of the first and the 3000th cycle (Figure 10b) further evidences the electrochemical stability of our device.

Based on the above analysis, our HSC exhibits high volumetric energy and power densities as well as impressive cycling life, which are extremely attractive for thin-film downsized energy storage. In particular, with both the anode and cathode nanostructured films growing directly from current collector, the fully binder-free HSC is expected to have good mechanical flexibility and may hold great promise in future smart and flexible electronic applications.

In summary, we have constructed a HSC device using MWCNT network film and LTO nanowire array grown directly on current collectors as cathode and anode, respectively. The HSC is entirely binder-free and additive-free, different from all previous HSCs. With a wide potential window of 0–3.0 V, our HSC has high volumetric energy densities comparable to that of commercial 4 V–500 μAh thin-film lithium batteries and maximum volumetric power density (565 mW cm⁻³) approaching that of the commercially available supercapacitors. To our knowledge, the maximum energy density (4.38 mWh cm⁻³) is among the highest value reported for super-capacitors based on thin-film electrodes fabricated directly on car-bon cloth. The HSC device also shows outstanding cycling stability of more than 3000 times. Our work unambiguously demonstrates that the binder-free HSC deserves exploration for thin-film downsized energy storage applications.

Methods

Fabrication of LTO nanowire array anode. The anode was prepared by a solid-state reaction from rutile TiO_2 (RTO) nanowire array template. To prepare the RTO array,

firstly, a piece of 2 cm × 2 cm carbon cloth (CeTech, thickness: ~0.33 mm) was placed into a ~2.2 vol% $TiCl_4$ alcohol solution for 12 h with subsequent annealing at 400°C for 1 h to produce the seeds[51]. Then, the seeded carbon cloth was immersed into a mixed solution containing 1.2–1.5 mL tetrabutyl titanate, 10 mL acetone and 10 mL hydrochloric acid, which was finally sealed in a Teflon-lined autoclave and maintained at 180°C for 2 h for hydrothermal growth. To transform the RTO into LTO, the as-grown RTO nanowire array was firstly wetted with 0.143 M lithium hydroxide (LiOH) sufficiently (~2.5 mL) and dried at 80°C, which was subsequently calcined at 700°C for 10 h in N_2 gas. After the transformation reaction between RTO and LiOH, the obtained LTO covered carbon cloth was ultrasonicated in deionized water for 5 s to dissolve the excess LiOH. The final sample was dried at 60°C for 24 h.

Fabrication of MWCNT film cathode. We grew MWCNT film by a facile CVD method with nickel as the catalyst and alcohols as the carbon source (repeated five times of growth). Typically, a piece of 2 cm × 2 cm carbon cloth was firstly infiltrated with a 0.5 M nickel nitrate hexahydrate solution and then dried in ambient air. The treated carbon cloth was then put at the center of a tube furnace and heated to 800°C for 30 minutes with a 15 mL mixed solution (ethanol and ethylene glycol with the volume ratio of 1 : 5) placed at the tube entrance under flowing argon atmosphere.

Characterizations. The morphology, microstructure and composition of the electrode samples were examined by scanning electron microscopy (SEM, JSM-6700F, 5 kV), transmission electron microscopy (TEM, JEM-2010FEF, 200 kV) and X-ray diffraction (XRD, Bruker D-8 Avance). The mass of electrode materials was measured on an AX/MX/UMX Balance (METTLER TOLEDO, maximum =5.1 g; d =1 μg).

Electrochemical testing. Half cells were assembled in an Ar-filled glovebox (Mbraun, Unilab, Germany) by using the directly-grown MWCNT film (~4 mg cm⁻²) or LTO nanowire array (~2.34 mg cm⁻²) as the working electrode, Li-metal circular foil as the reference/counter electrode, microporous polypropylene membrane as separator (~16 μm thickness), and 1 M solution of $LiPF_6$ in ethylene carbonate (EC) and diethyl carbonate (DEC) (1 : 1 by volume) as the electrolyte. Encapsulated full-cell HSC was fabricated by using MWCNT film as cathode and LTO nanowire array as anode while the separator and electrolyte are the same to those in half-cells. Two Pt wires were connected respectively with the cathode and anode for external circuits' connection. All cells were aged for 10 hours before electrochemical tests. The electrochemical performance was tested on multichannel battery tester (Neware, Shenzhen) and electrochemical workstation (CS310, Wuhan) at room temperature. The areal capacitance of MWCNT film electrode and HSC device was calculated accordingly to equations $C = \frac{I \times \Delta t}{\Delta V \times S}$, where I is the constant discharge current, Δt is the discharging time, ΔV is the voltage drop upon discharging (excluding the IR drop), and S is the geometrical area of the electrode or the device. For LTO battery anode, the areal capacity was obtained using $Q = I \times \Delta t$. The volumetric energy and powder densities of the device were calculated based on $E = \frac{\int IV(t)dt}{T_{cell}}$ and $P = \frac{E}{\Delta t}$, where $V(t)$ is discharging voltage at t, $d(t)$ is time differential, and T_{cell} is the volume of HSC device (including current collector, anode, cathode, separator, and electrolyte. Device area: ~4 cm², total measured thickness: ~691 μm). The gravimetric capacitance, gravimetric energy and power densities were evaluated based on the mass of active electrode materials (replacing the area S or volume T_{cell} in the above formulas with mass).

1. Tarascon, J. M. & Armand, M. Issues and Challenges Facing Rechargeable Lithium Batteries. *Nature* **414**, 359–367 (2001).
2. Miller, J. R. & Simon, P. Electrochemical Capacitors for Energy Management. *Science* **321**, 651–652 (2008).
3. Burke, A. Ultracapacitors: Why, How and Where is The Technology. *J. Power Sources* **91**, 37–50 (2000).
4. Bruce, P. G., Scrosati, B. & Tarascon, J. M. Nanomaterials for Rechargeable Lithium Batteries. *Angew. Chem., Int. Ed.* **47**, 2930–2946 (2008).
5. Yan, J., Wang, Q., Wei, T. & Fan, Z. J. Recent Advances in Design and Fabrication of Electrochemical Supercapacitors with High Energy Densities. *Adv. Energy. Mater.* **4** DOI: 10.1002/aenm.201300816 (2014).
6. Xia, H., Li, B. & Li, L. 1.8 V Symmetric Supercapacitors Developed Using Nanocrystalline Ru Films as Electrodes. *RSC Adv.* **4**, 11111–11114 (2014).
7. El-Kady, M. F., Strong, V., Dubin, S. & Kaner, R. B. Laser Scribing of High-Performance and Flexible Graphene-Based Electrochemical Capacitors. *Science* **335**, 1326–1330 (2012).
8. Yu, D. *et al.* Scalable Synthesis of Hierarchically Structured Carbon Nanotube-Graphene Fibres for Capacitive Energy Storage. *Nat. Nanotech.* **9**, 555–562 (2014).
9. Kong, D. Z. *et al.* Three-Dimensional Co₃O₄@MnO₂ Hierrchical Nanoneedle Arrays: Morphology Control and Electrochemical Energy Storage. *Adv. Funct. Mater.* **24**, 3815–3826 (2014).
10. Wang, Y. Q. *et al.* Rutile-TiO₂ Nanocoating for a High-Rate Li₄Ti₅O₁₂ Anode of a Lithium-Ion Battery. *J. Am. Chem. Soc.* **134**, 7874–7879 (2012).
11. Li, Y., Tan, B. & Wu, Y. Mesoporous Co₃O₄ Nanowire Arrays for Lithium Ion Batteries with High Capacity and Rate Capability. *Nano Lett.* **8**, 265–270 (2008).

12. Huang, M. et al. Self-Assembly of Mesoporous Nanotubes Assembled from Interwoven Ultrathin Birnessite-type MnO_2 Nanosheets for Asymmetric Supercapacitors. Sci. Rep. 4, 3878 (2014).

13. Lu, X. et al. H-TiO_2@MnO_2//H-TiO_2@C Core–Shell Nanowires for High Performance and Flexible Asymmetric Supercapacitors. Adv. Mater. 25, 267–272 (2013).

14. Ji, J. et al. Nanoporous $Ni(OH)_2$ Thin Film on 3D Ultrathin-Graphite Foam for Asymmetric Supercapacitor. ACS Nano 7, 6237–6243 (2013).

15. Yan, W. et al. Lithographically Patterned Gold/Manganese Dioxide Core/Shell Nanowires for High Capacity, High Rate, and High Cyclability Hybrid Electrical Energy Storage. Chem. Mater. 24, 2382–2390 (2012).

16. Vlad, A. et al. Hybrid supercapacitor-battery materials for fast electrochemical charge storage. Sci. Rep. 4, 4315 (2014).

17. Xu, J. et al. Flexible Asymmetric Supercapacitors Based Upon Co_9S_8 Nanorod//Co_3O_4@RuO_2 Nanosheet Arrays on Carbon Cloth. ACS Nano 7, 5453–5462 (2013).

18. Yang, P. et al. Low-Cost High-Performance Solid-State Asymmetric Supercapacitors Based on MnO_2 Nanowires and Fe_2O_3 Nanotubes. Nano Lett. 14, 731–730 (2014).

19. Liu, J. et al. Co_3O_4 Nanowire@MnO_2 Ultrathin Nanosheet Core/Shell Arrays: A New Class of High-Performance Pseudocapacitive Materials. Adv. Mater. 23, 2076–2081 (2011).

20. Zhou, C., Zhang, Y., Li, Y. & Liu, J. Construction of High-Capacitance 3D CoO@Polypyrrole Nanowire Array Electrode for Aqueous Asymmetric Supercapacitor. Nano Lett. 13, 2078–2085 (2013).

21. Wang, Q., Wen, Z. H. & Li, J. H. A Hybrid Supercapacitor Fabricated with a Carbon Nanotube Cathode and a TiO_2–B Nanowire Anode. Adv. Funct. Mater. 16, 2141–2146 (2006).

22. Niu, Z. Q. et al. Compact-Designed Supercapacitors Using Free-Standing Single-Walled Carbon Nanotube Films. Energy Environ. Sci. 4, 1440–1446 (2011).

23. Zhang, F. et al. A High-Performance Supercapacitor-Battery Hybrid Energy Storage Device Based on Graphene-Enhanced Electrode Materials with Ultrahigh Energy Density. Energy Environ. Sci. 6, 1623–1632 (2013).

24. Choi, H. S., Im, J. H., Kim, T., Park, J. H. & Park, C. R. Advanced Energy Storage Device: a Hybrid BatCap System Consisting of Battery–Supercapacitor Hybrid Electrodes Based on $Li_4Ti_5O_{12}$-Activated-Carbon Hybrid Nanotubes. J. Mater. Chem. 22, 16986–16993 (2012).

25. Kim, H. et al. A Novel High-Energy Hybrid Supercapacitor with an Anatase TiO_2–Reduced Graphene Oxide Anode and an Activated Carbon Cathode. Adv. Energy. Mater. 3, 1500–1506 (2013).

26. Wang, Y. & Xia, Y. A New Concept Hybrid Electrochemical Surpercapacitor: Carbon/$LiMn_2O_4$ Aqueous System. Electrochem Commun 7, 1138–1142 (2004).

27. Hu, X., Deng, Z., Suo, J. & Pan, Z. A High Rate, High Capacity and Long Life ($LiMn_2O_4$+AC)/$Li_4Ti_5O_{12}$ Hybrid Battery–Supercapacitor. J. Power Sources 187, 635–639 (2009).

28. Chen, Z. et al. High-Performance Supercapacitors Based on Intertwined CNT/V_2O_5 Nanowire Nanocomposites. Adv. Mater. 23, 791–795 (2011).

29. Liu, X. et al. Silicon/copper dome-patterned electrodes for high-performance hybrid supercapacitors. Sci. Rep. 3, 3183 (2013).

30. Naoi, K., Ishimoto, S., Miyamoto, J. I. & Naoi, W. Second Generation 'Nanohybrid Supercapacitor': Evolution of Capacitive Energy Storage Devices. Energy Environ. Sci. 5, 9363–9373 (2012).

31. Lim, E. et al. Advanced Hybrid Supercapacitor Based on a Mesoporous Niobium Pentoxide/Carbon as High-Performance Anode. ACS Nano 8, 8968–8978 (2014).

32. Lei, Y. et al. Porous mesocarbon microbeads with graphitic shells: constructing a high-rate, high-capacity cathode for hybrid supercapacitor. Sci. Rep. 3, 2477 (2013).

33. Jiang, J. et al. Recent Advances in Metal Oxide-Based Electrode Architecture Design for Electrochemical Energy Storage. Adv. Mater. 24, 5166–5180 (2012).

34. Zhang, X. et al. High-Power and High-Energy-Density Flexible Pseudocapacitor Electrodes Made from Porous CuO Nanobelts and Single-Walled Carbon Nanotubes. ACS Nano 5, 2013–2019 (2011).

35. Chabi, S., Peng, C., Hu, D. & Zhu, Y. Ideal Three-Dimensional Electrode Structures for Electrochemical Energy Storage. Adv. Mater. 26, 2440–2445 (2014).

36. Yang, P. H. & Mai, W. J. Flexible Solid-State Electrochemical Supercapacitors. Nano Energy 8, 274–290 (2014).

37. Beidaghi, M. & Gogotsi, Y. Capacitive Energy Storage in Micro-Scale Devices: Recent Advances in Design and Fabrication of Micro-Supercapacitors. Energy Environ. Sci. 7, 867–884 (2014).

38. Zhou, G. M., Li, F. & Cheng, H. M. Progress in Flexible Lithium Batteries and Future Prospects. Energy Environ. Sci. 7, 1307–1338 (2014).

39. Gwon, H. et al. Recent Progress on Flexible Lithium Rechargeable Batteries. Energy Environ. Sci. 7, 538–551 (2014).

40. Lu, X., Yu, M., Wang, G., Tong, Y. & Li, Y. Flexible Solid-State Supercapacitors: Desigh, Fabrication and Applications. Energy Environ. Sci. 7, 2160–2180 (2014).

41. Amatucci, G. G., Badway, F., Du Pasquier, A. & Zheng, T. An Asymmetric Hybrid Nonaqueous Energy Storage Cell. J. Electrochem. Soc. 148, A930–A939 (2001).

42. Jiang, J., Li, Y., Liu, J. & Huang, X. Building One-Dimensional Oxide Nanostructure Arrays on Conductive Metal Substrates for Lithium-Ion Battery Anodes. Nanoscale 3, 45–58 (2011).

43. Chan, C. K. et al. High-Performance Lithium Battery Anodes using Silicon Nanowires. Nat Nanotechnol. 3, 31–35 (2008).

44. Chen, H., Hu, L., Chen, F. M., Yan, Y. & Wu, L. M. Nickel–Cobalt Layered Double Hydroxide Nanosheets for High-performance Supercapacitor Electrode Materials. Adv. Funct. Mater. 24, 934–943 (2014).

45. Giri, S., Ghosh, D. & Das, C. K. Growth of Vertically Aligned Tunable Polyaniline on Graphene/ZrO_2 Nanocomposites for Supercapacitor Energy-Storage Application. Adv. Funct. Mater. 24, 1312–1324 (2014).

46. Wang, K. et al. An All-Solid-State Flexible Micro-supercapacitor on a Chip. Adv. Energy. Mater. 1, 1068–1072 (2011).

47. Xia, X. H. et al. A New Type of Porous Graphite Foams and Their Integrated Composites with Oxide/Polymer Core/Shell Nanowires for Supercapacitors: Structural Design, Fabrication, and Full Supercapacitor Demonstrations. Nano Lett. 14, 1651–1658 (2014).

48. Yang, P. et al. Hydrogenated ZnO Core–Shell Nanocables for Flexible Supercapacitors and Self-Powered Systems. ACS Nano 7, 2617–2626 (2013).

49. Jiang, J. et al. CNT/Ni hybrid nanostructured arrays: synthesis and application as high-performance electrode materials for pseudocapacitors. Energy Environ. Sci. 4, 5000–5007 (2011).

50. Xiao, X. et al. WO_{3-x}/MoO_{3-x} Core/Shell Nanowires on Carbon Fabric as an Anode for All-Solid-State Asymmetric Supercapacitors. Adv. Energy. Mater. 2, 1328–1332 (2012).

51. Wang, Z. et al. Transferable and Flexible Nanorod-Assembled TiO_2 Cloths for Dye-Sensitized Solar Cells, Photodetectors, and Photocatalysts. ACS Nano 5, 8412–8419 (2011).

52. Lu, X. et al. High Energy Density Asymmetric Quasi-Solid-State Supercapacitor Based on Porous Vanadium Nitride Nanowire Anode. Nano Lett. 13, 2628–2633 (2013).

53. Kaempgen, M., Chan, C. K., Ma, J., Cui, Y. & Gruner, G. Printable Thin Film Supercapacitors Using Single-Walled Carbon Nanotubes. Nano Lett. 9, 1872–1876 (2009).

54. Yu, L., Wu, H. B. & Lou, X. W. Mesoporous $Li_4Ti_5O_{12}$ Hollow Spheres with Enhanced Lithium Storage Capability. Adv. Mater. 25, 2296–2300 (2013).

55. Kim, J. & Cho, J. Spinel $Li_4Ti_5O_{12}$ Nanowires for High-Rate Li-Ion Intercalation Electrode. J. Electrochem. Solid State Lett. 10, A81–A84 (2007).

56. Zhao, L., Hu, Y. S., Li, H., Wang, Z. X. & Chen, L. Q. Porous $Li_4Ti_5O_{12}$ Coated with N-Doped Carbon from Ionic Liquids for Li-Ion Batteries. Adv. Mater. 23, 1385–1388 (2011).

57. Sun, Y. et al. X. Direct Atomic-Scale Confirmation of Three-phase Storage Mechanism in $Li_4Ti_5O_{12}$ Anodes for Room-Temperature Sodium-Ion Batteries. Nat. Commun. 4, 1870 (2013).

58. Shen, L. F., Uchaker, E., Zhang, X. G. & Cao, G. Z. Hydrogenated $Li_4Ti_5O_{12}$ Nanowire Arrays for High Rate Lithium Ion Batteries. Adv. Mater. 24, 6502–6506 (2012).

59. Kang, E. et al. Highly Improved Rate Capability for a Lithium-Ion Battery Nano-$Li_4Ti_5O_{12}$ Negative Electrode via Carbon-Coated Mesoporous Uniform Pores with a Simple Self-Assembly Method. Adv. Funct. Mater. 21, 4349–4357 (2011).

60. Ganapathy, S. & Wagemaker, M. Nanosize Storage Properties in Spinel $Li_4Ti_5O_{12}$ Explained by Anisotropic Surface Lithium Insertion. ACS Nano. 6, 8702–8712 (2012).

Acknowledgments

Author contributions

J.L., W.Z. and Y.L. designed project and carried out data analyses. W.Z. and C.W. did the experiments. J.L. and W.Z. co-wrote the manuscript.

Additional information

Competing financial interests: The authors declare no competing financial interests.

How to cite this article: Zuo, W., Wang, C., Li, Y. & Liu, J. Directly Grown Nanostructured Electrodes for High Volumetric Energy Density Binder-Free Hybrid Supercapacitors: A Case Study of CNTs//$Li_4Ti_5O_{12}$. Sci. Rep. 5, 7780; DOI:10.1038/srep07780 (2015).